Strong Coupling of Tamm Plasmons and Fabry-Perot Modes in a One-Dimensional Photonic Crystal Heterostructure

Jie Yang,[1,2] Haoran Zhang,[1,2] Tao Wang[1,2,*] Israel De Leon,[3] Remo Proietti Zaccaria,[4] Haoliang Qian,[5] Hongsheng Chen,[5] and Gaofeng Wang[1,2]

[1]*Engineering Research Center of Smart Microsensors and Microsystems of MOE, Hangzhou Dianzi University, Hangzhou 310018, China*

[2]*School of Electronics and Information, Hangzhou Dianzi University, Hangzhou 310018, China*

[3]*School of Engineering and Sciences, Tecnologico de Monterrey, Monterrey, Nuevo León 64849, Mexico*

[4]*Cixi Institute of Biomedical Engineering, Ningbo Institute of Materials Technology and Engineering, Chinese Academy of Sciences; Italian Institute of Technology, via Morego 30, Genova 16163, Italy*

[5]*Interdisciplinary Center for Quantum Information, College of Information Science and Electronic Engineering, Zhejiang University, Hangzhou 310027, China*

The coupling between multiple modes in subwavelength scale has attracted a lot of attention due to the interesting physics favored by the enhancement of light-matter interaction. In this contribution, we propose a planar hybrid plasmonic-photonic crystal structure, which enables the tunable coupling between Tamm plasmon-polariton and Fabry-Perot cavity modes. Then, a strong coupling can be achieved through evoking the Tamm-mode dependence of the top-layer thickness of the hybrid structure, which is indicated by an anticrossing with a spectrum splitting of 9.298 meV. The effect enables the spatial confinement of polaritons and the formation of hybrid one-dimensional plasmon-polariton modes. In order to account for the splitting of the orthogonally polarized resonances, a detailed investigation on the TE-TM splitting is also performed through the angular-dependence analysis. We note that the value of the TE-TM splitting strongly depends on the thicknesses of dielectric layer and the distance between two distributed Bragg reflector (DBR) stacks. We show that the cavity modes are extremely sensitive to the distance between the DBR stacks and propose using this feature for strain sensing. Thus, our structure may not only offer a platform for study of interesting physics (e.g., spin optronics), but may also provide a route for high-accuracy strain sensors.

I. INTRODUCTION

The enhancement of light-matter interactions in photonic structures is not only useful from a fundamental physics point of view [1–3], but also for numerous potential applications [4–10]. In principle, these applications are generally based on the excitation of optical resonant states, including Fabry-Perot (FP) cavity modes [11], whispering-gallery modes (WGM) [12], and surface plasmon polariton (SPP) modes [13]. Different from the first two kinds of cavity resonances, SPPs are electromagnetic surface states generated at the interface between a metal and a dielectric layer, which allow light localization on scales beyond the diffraction limit [2,14,15]. Because of their ability to concentrate light at the nanoscale, SPPs are useful for many applications, such as sensing [16], surface-enhanced Raman scattering [17], and circuitry [18,19].

Recently, another type of surface state, known as Tamm plasmon polaritons (TPPs), have been reported to exist at the metal-dielectric layers' interface, exhibiting low propagation loss [20,21]. In comparison with the conventional SPPs, TPPs can be excited without the use of a prism, grating coupling or an alternative surface-structuring approach, using both TE- and TM-polarized light irrespective of their angle of incidence [22–24]. Thus, those features enable TPPs to be promising for various applications in optical filters [25,26], Tamm plasmon lasers [27–29], sensors [30,31], thermal emitters [32,33], and other kinds of light-emitting devices [34].

Apart from the aforementioned properties, TPPs can be strongly coupled with other resonant modes (e.g., FP cavity mode), creating "hybrid" systems. The coupling of multiple resonant modes has attracted considerable attention in the last few decades, and several studies have been reported on their collective properties. For instance, the phenomenon of strong coupling between two cavity modes

*wangtao@hdu.edu.cn

014056-1

and one exciton mode was observed in coupled semiconductor microcavities [35]; the ultrastrong coupling limit of multiple modes was theoretically depicted in cavity quantum electrodynamics [36]; the strong exciton-photon coupling in metal-clad microcavities was demonstrated and a 110-meV Rabi splitting was achieved at room temperature [37].

The interaction between TPP and FP cavity modes is different from the conventional strong coupling observed in coupled microcavities [35], which brings more interesting hybridization or frequency-splitting characteristics, for instance, the enhancement of magneto-optical effects has been observed recently [38]. In addition, the strong coupling between TPP and FP modes can be used to sharpen the resonances, which can be exploited for practical applications, such as optical sensing and filtering [39]. What is more, the realization of multimode interaction in one-dimensional (1D) photonic crystal heterostructures may favor an ultracompact integrated optical circuit [40].

In this contribution, we present a platform for tailoring the coupling between Tamm plasmon and Fabry-Perot modes through a planar metal-distributed Bragg reflector-(DBR) based structure. Through the realization of dual DBRs physically coupled to a metallic layer (see Fig. 1), TPP and FP cavity modes are excited simultaneously in the wavelength range of interest. In comparison with structures such as the metal grating capped DBRs [41,42], our design is much simpler from the fabrication point of view. The introduction of an addition DBR stack enables another flexibility for the multiple modes' coupling.

Our theoretical and numerical analysis shows that mode coupling can be tuned by adjusting the thickness of the dielectric layer and the distance between two DBR stacks (i.e., GDBR$_1$ in Fig. 1), resulting in perfect absorption at multiple wavelengths, in spacial electromagnetic (EM) field tailoring as well as in the formation of three polaritonlike bands with two distinct frequency splittings. The

TE-TM splitting is investigated through angular dependence analysis, a splitting that is responsible for various phenomena in the emerging field of spin optronics [43]. In addition, taking advantage of the dynamical coupling between the TPP and FP modes caused by the distance changing between two DBR stacks, we propose a strain sensor capable of detecting nanometric changes in the cavity's length induced by pressure, heat, or other compressive and expansive forces, which may be very promising for applications such as high-accuracy strain sensing.

II. STRUCTURE DESIGN AND SIMULATION METHOD

A graphical illustration of the proposed metal-DBR structure is shown in Fig. 1. It consists of two groups of DBRs (indicated as GDBR$_1$ and GDBR$_2$) separated by a distance D. The two DBRs are made of Al$_{0.9}$Ga$_{0.1}$As/GaAs bilayers, GDBR$_1$ with $N = 20$ bilayers and GDBR$_2$ with $N = 19.5$. The thicknesses of Al$_{0.9}$Ga$_{0.1}$As and GaAs layers are denoted by D_L and D_H, respectively. These values are selected to satisfy the quarter-wave condition [44] as $\lambda/4 = n_L D_L = n_H D_H$, where λ is the emission wavelength of device. For sensing applications, the space between the DBRs can be filled either with gas or liquid. Here, we simply consider it as gaseous medium with refractive index n_a equal to 1.00. Along z direction, one dielectric layer with D_s thickness and the same refractive index of In-Ga-As-P, but no loss and dispersion, is deposited on the top of GDBR$_1$. Finally, a thin Ag layer with complex permittivity is deposited on the top of the dielectric layer, and its thickness is represented by t_{Ag}. The permittivities of the materials employed in this study are listed in Table I.

The finite-difference time-domain (FDTD) method is adopted to numerically simulate the optical response of the device. Within the calculation, periodic boundary conditions are set around the sides of the device, while perfectly matched layer (PML) boundary conditions are used on the top of the Ag layer and the bottom of the substrate. The spatial mesh grids in Ag and dielectric layers are set as $\Delta z = 2$ nm, $\Delta x = \Delta y = 5$ nm. Then, auto nonuniform with a minimum mesh size of 0.25 nm is used for the other layers. A plane wave along $-z$ direction is used as the excitation source, having a wavelength span of 800 nm.
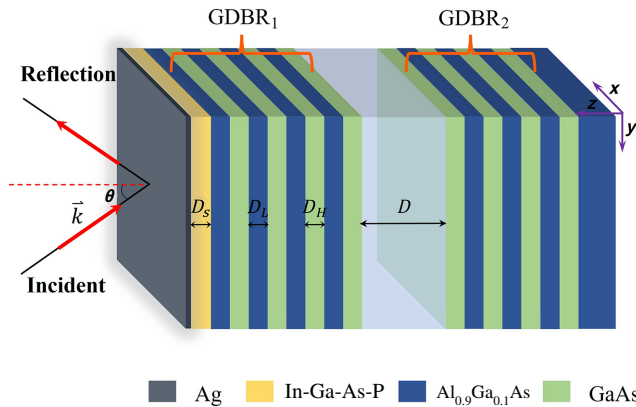

FIG. 1. Structure diagram of the metal dual DBR-based structure: GDBR$_1$ is made up by 20 pairs Al$_{0.9}$Ga$_{0.1}$As/GaAs DBR films, and GDBR$_2$ has 19.5 pairs.

TABLE I. Geometrical and material parameters of the proposed devices.

Material	Dimension	Refractive index
Ag	$t_{Ag} = 18$ nm	$n_{Ag} = 0.16 + i11.35$
In-P-Ga-As	$D_s = 165$ nm	$n_S = 3.3$
GaAs	$D_H = 114$ nm	$n_H = 3.37$
Al$_{0.9}$Ga$_{0.1}$As	$D_L = 130$ nm	$n_L = 2.97$
Air	∞ (analyte)	$n_a = 1.00$

III. HYBRIDIZATION BETWEEN FP AND TPP MODES

The reflectance spectrum and the electric field intensity profiles for normal TE-polarized incident radiation ($\theta = 0$ in Fig. 1), are calculated based on the transfer matrix method [22,45]. The results, based on the parameters in Table I, are shown in Fig. 2. Here, three different scenarios are envisioned. The first case is about a structure consisting of GDBR$_1$, single silver layer, and GDBR$_2$ ($D_s = 165$ nm in Fig. 1). The results obtained for such a structure are shown in Figs. 2(a) and 2(d). In the reflection spectrum we observe a spectral feature with central wavelength of 1507 nm and linewidth (full width at half maximum) of 8 nm [Fig. 2(a)]. Furthermore, the field distribution associated with this spectral feature peaks at the silver layer ($z = 10$ μm) and exponentially decays from it along $-z$ (excitation) direction [Fig. 2(d)], suggesting that it is a Tamm plasmon polariton mode [32]. The formation of the TPP mode is due to the coupling effect between SPPs and the optical Tamm state (OTS) [46]. In detail, when the resonance tunneling of SPPs goes through the Tamm state, a narrow peak will appear from the reflectance spectrum for the region where the band gaps overlap.

The second scenario consists of a structure formed by GDBR$_1$ and GDBR$_2$ with $D = 345$ nm, but with no silver layer. The results obtained for such a structure are shown in Figs. 2(b) and 2(e). In this case, the reflectance spectrum exhibits a spectral feature centered at the same wavelength as the Tamm state, but with a much narrower linewidth of 1.60 nm [Fig. 2(b)], suggesting a low radiative-loss cavity mode. Furthermore, the electric field profile associated with this spectral feature peaks at the region between the two DBRs, with symmetric exponential decay into the DBRs, indicating that it is a FP mode.

Finally, the third scenario considers the structure shown in Fig. 1 with $D = 345$ nm. The results for such a structure are shown in Figs. 2(c) and 2(f). The reflection spectrum shows two spectral features with central wavelengths shifted to shorter and longer wavelengths compared to the previous two cases. This large wavelength shift is indicative of a strong coupling between the FP and TPP modes [47]. From the electric field distribution, we note that the confinement not only occurs at the interface between Ag and GDBR$_1$, but also can be observed at the interface between two DBR stacks, which is coherent with the presence of two broad peaks in Fig. 2(f).

Interestingly, the degree coupling strength of these modes can be controlled by tuning the parameter D_s, which describes the thickness of the spacer layer between the silver film and GDBR$_1$. Figure 3(a) shows the reflectance spectra of the mixed structure (Ag layer/dielectric layer/GDBR$_1$/air/GDBR$_2$) as a function of D_s. For energies between 0.79 and 0.85 eV, one can observe two anticrossing points corresponding to values of $D_s = 165$ and 208 nm, for which the TPP and FP modes of the structure couple. In particular, for $D_s = 165$ nm, a frequency splitting of 9.298 meV is achieved, a result much larger than the previous reports [48]. Figure 3(b) depicts the bare FP mode (black circle line) and Tamm mode (red circles) when crossing each other at $D_s = 165$ nm, together with the hybrid mode characterized by the typical anticrossing behavior (blue triangles) occurring under strong coupling condition. The bare FP mode is obtained from a structure without Ag layer and the bare TPP is obtained by adding a Ag layer and making $D = 0$.

In order to better understand the hybridization process between the FP and TPP modes within our system, in Fig. 4(a) we plot the reflectance spectra for values of D_s equal to 155, 165, and 175 nm, respectively. For $D_s = 155$ nm, two reflection peaks appear at 1498 and 1513 nm. The short-wavelength mode belongs to the upper-branch hybrid mode [see Fig. 3(b)]. Its resonance wavelength and field distribution resembles those of the bare TPP mode, and hence we refer to it as TPP-like mode. The
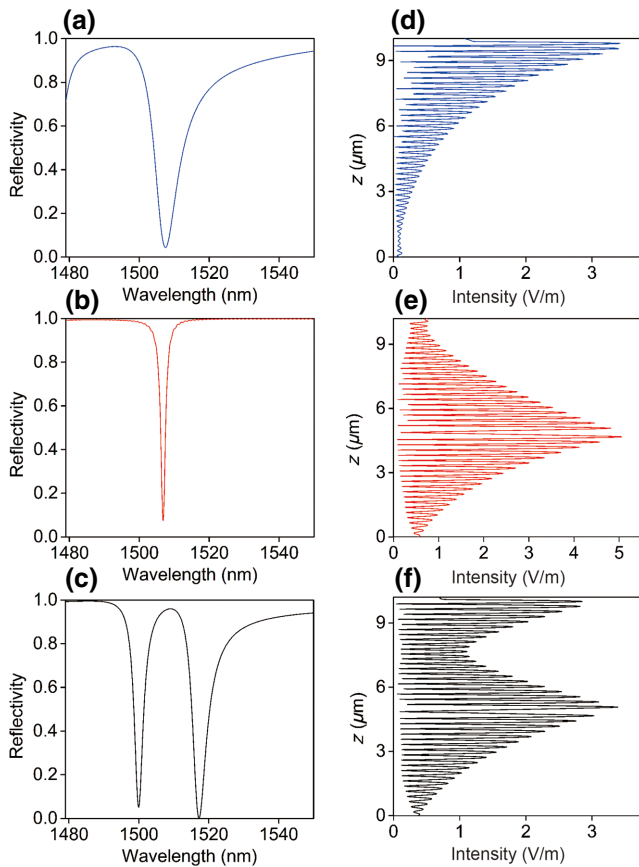
FIG. 2.   (a)–(c) Reflection spectra of the photonic structure with the metallic layer (TP mode), without the metallic layer (bare cavity mode), and with both the metallic layer and spacing (hybrid TP-cavity modes), respectively; (d)–(f) electric field profiles along z direction sampled at $x = 0$.
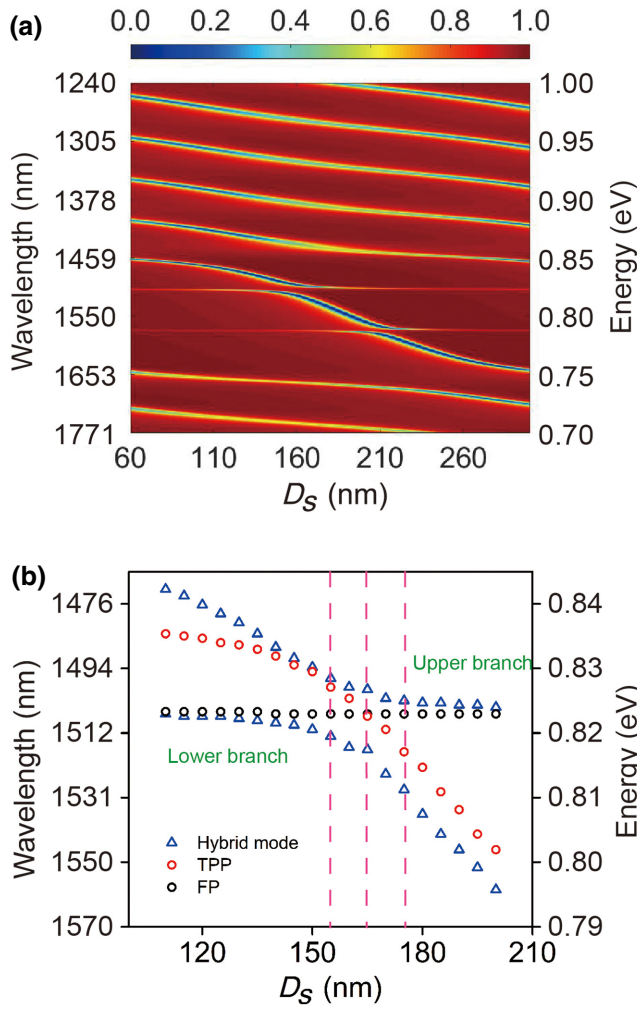
FIG. 3. (a) Reflectance spectra mapping of the mixed structure; (b) analytical dispersion relations of FP, TPP, and hybrid modes.

FIG. 4. (a) Reflectance spectra obtained when $D_s = 155$, 165, and 175 nm; (b) the corresponding energy diagrams for mode hybridization.

long-wavelength mode belongs to the lower-branch hybrid mode. It resembles the bare FP mode, having a similar field distribution and resonance wavelength and hence we refer to it as FP-like mode. For $D_s = 175$ nm, however, the nature of the hybrid modes is inverted. The short-wavelength mode, located on the lower branch, becomes the TPP-like mode, while the long-wavelength mode, located on the upper branch, becomes the FP-like mode. For all cases, the field distributions of FP-like and TPP-like modes resemble those of their nonhybrid counterparts; in other words, the fields of FP-like modes peak in the region between the DBRs, while those of TPP-like modes peak near the metal surface. As D_s is increased, the two hybrid modes not only undergo a redshift, but their reflectivities are also modified. Finally, for $D_s = 165$ nm, they have almost the same reflectivity. For this case, the bare TPP and bare FP modes have the same resonant wavelength, leading to the strongest coupling. Indeed, both hybrid modes
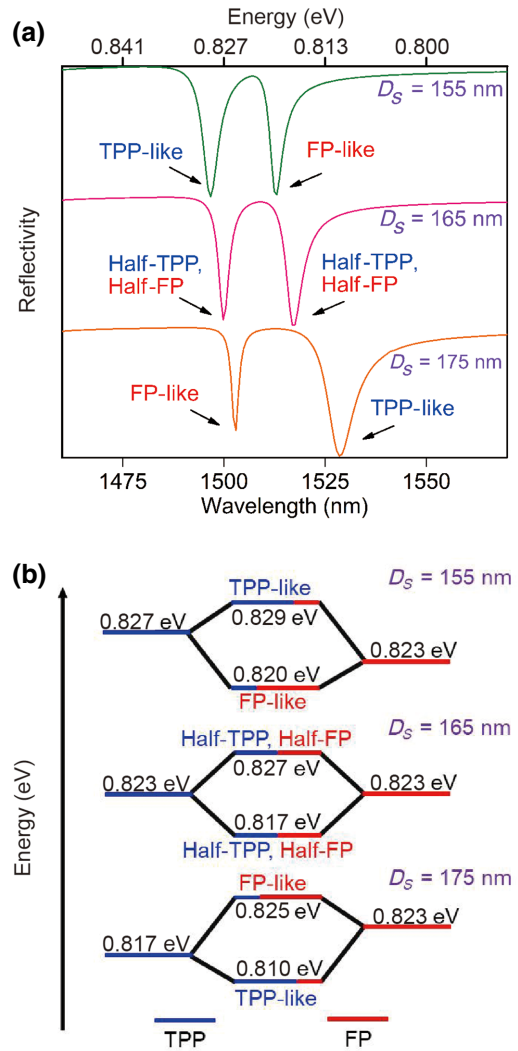
show strong TPP and FP characteristics. Figure 4(b) displays the corresponding energy diagrams, which provide a dynamical interaction process between TPP and FP modes.

IV. PARABOLIC POLARIZATION SPLITTING

To further gain physical insights the coupling between FP and TPP modes, we study the angular-resolved reflectance spectra obtained by using TE (E∥y direction) and TM (E∥x direction) polarized plane-wave excitations, and investigate the resonance splitting for different linear polarization states (often referred to as TE-TM splitting). This type of analysis is in fact a characterization method when we consider the metal-DBR contact in the microcavity laser device. The TE-TM splitting effect is also responsible for various phenomena in the emerging field of
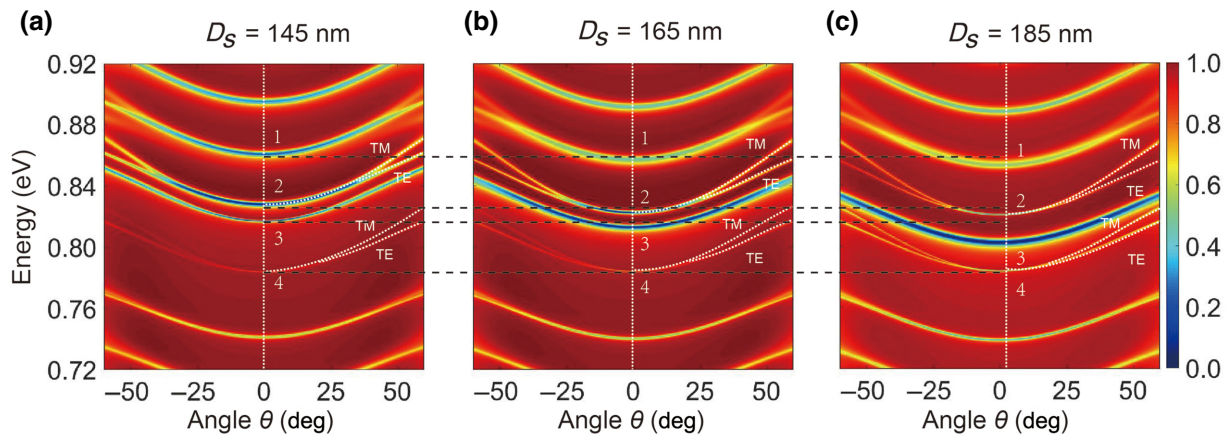
FIG. 5.   Angular-resolved reflectance spectra for TE- and TM-polarized illumination taking $D_s = 145$ nm (a), 165 nm (b), and 185 nm (c). In (a), positions 1 to 4 correspond to FP cavity mode, FP-like mode, TPP-like mode, and FP cavity mode, respectively. In (b),(c), the positions from 1 to 4 correspond to the same modes. The black dashed lines show the shifting of different modes.

spin optronics, including the "all optical" spin Hall effect and the formation of polarized patterns [49].

Figure 5 displays the calculated angle-resolved reflectance spectra for our structure when $D_s = 145$, 165, and 185 nm. We clearly observe that all the modes exhibit identical parabolic dispersion curve irrespective of the excitation polarization. For normal incidence ($\theta = 0$ in Fig. 1) and when $D_s = 145$ nm, the FP-like mode and the TPP-like mode are characterized by energies equal to 0.8285 eV [position 2 in Fig. 5(a)] and 0.8174 eV [position 3 in Fig. 5(a)], respectively. In addition, two FP cavity modes can be identified at the energies 0.8602 eV [position 1 in Fig. 5(a)] and 0.7844 eV [position 4 in Fig. 5(a)]. The FP mode at position 1 is caused by the cavity created by the Ag layer and GDBR$_1$, while the FP mode at position 4 is due to the cavity formed by GDBR$_1$ and GDBR$_2$. With the increase of D_s, the modes at position 1 (FP), 2 (FP-like), and 3 (TPP-like) experience a redshifting, but the mode at position 4 (FP) keeps a constant energy level, as shown by the reference dashed lines in Fig. 5.

For large incident angles, all the modes experience redshifting. The reason is based on the relation $\delta = 2\pi n d \cos\theta / \lambda$ (where d is the cavity thickness), where the energy (which is proportional to the inverse of λ) of the modes needs to increase to maintain a fixed phase shift (δ) with the increase of angle (θ). Apart from the TPP-like mode at position 3, all the FP (like) modes display a splitting between TM- (upper branch) and TE polarization (lower branch) except at normal incidence where they are degenerative. The absence of a TE-TM splitting for the TPP-like mode can be understood by recalling that this kind of mode is formed by the light being reflected by the DBRs, hence no effect is associated to the incident light (i.e., the incident angle). In addition, we find that the onset of TE-TM splitting for different modes shifts to larger angles by increasing the energy.

When D_s goes up to 165 nm [Fig. 5(b)], the FP and TPP modes are strongly coupled with each other, and the energies associated to the corresponding hybrid modes approach the energy of the cavity mode at position 4. At the same time, we find the TE-TM splitting of the FP cavity mode at position 1 is less pronounced due to the increased cavity length, while the FP-like mode at position 2 and the cavity mode at position 4 show increased TE-TM splittings. A further increase of D_s to 185 nm [Fig. 5(c)], returns a weaker coupling between the FP and TPP modes. In addition, we note that the TE-TM splittings for FP-like mode and cavity mode at position 4 become even larger.

Figure 6(a) shows the reflectance spectrum of the structure with $D_s = 165$ nm under normal incidence ($\theta = 0$). We further identify the properties of different modes by combining the spectral linewidth with the corresponding electric field intensity distribution profiles [Figs. 6(b)–6(e)]. The mode at position 1 shows a broad linewidth together with a reduced field intensity, and the field intensity is smaller, which is due to the weak confinement of the cavity composed of Ag layer and GDBR$_1$. The mode at position 2 possesses much narrower linewidth, and the field intensity profile indicates the typical feature of a FP-like mode: more energy reaches the GDBR$_1$-GDBR$_2$ interface, in particular at the bottom of GDBR$_1$, thus enabling a stronger FP mode component. By contrast, the mode at position 3 has a larger linewidth, and the profile suggests the most energy is located at Ag/GDBR$_1$ interface, therefore, a stronger TPP mode component is presented. Meanwhile, a weaker FP mode component is visible at the GDBR$_1$-GDBR$_2$ interface. Clearly, the mode at position 4 has a very narrow linewidth, indicating a high-quality factor. Correspondingly, the field profile displays the property of a bare Fabry-Perot cavity mode—strong confinement in the middle part of the two DBR stacks, homogeneously decaying to both sides.
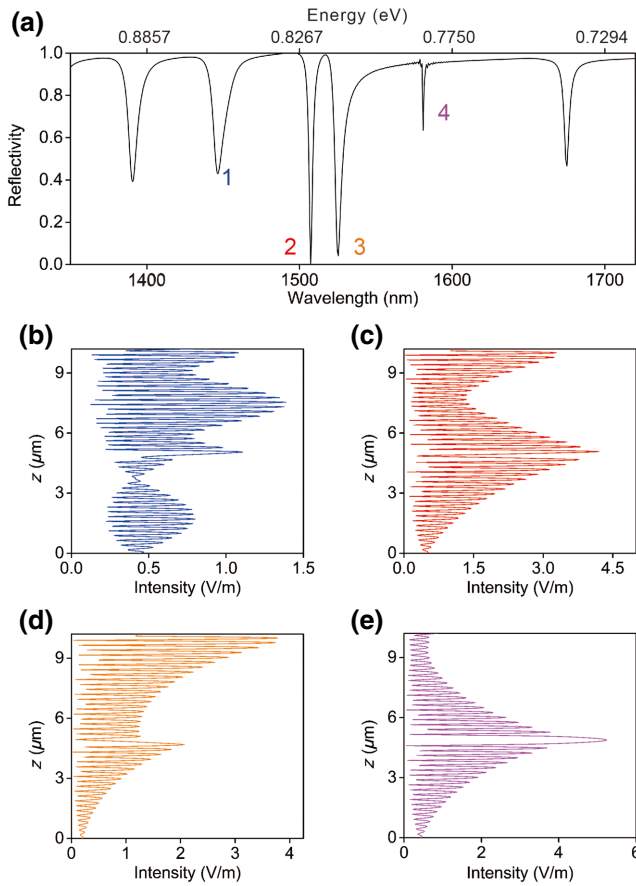
FIG. 6. (a) Reflectance spectrum of designed structure with $D_s = 165$ nm under normal incidence. (b)–(e) Field intensity distributions in (x, z) plane of different modes: mode 1 (b); mode 2 (c); mode 3 (d); mode 4 (e).

Finally, we also investigate the angular-resolved reflectance spectra by changing the distance D between the two DBR stacks, which is referred to another cavity.

As shown in Fig. 7, all the modes exhibit similar parabolic dispersion curves by changing the parameter of D. Furthermore, the modes exhibit a redshift with increase of the incident angle θ, regardless of TE- or TM-polarized waves. Under the condition of normal incidence ($\theta = 0$ in Fig. 1), the modes at position 1 (FP), 2 (FP-like), and 4 (FP) show a redshift with the increase of D_s, but the mode at position 3 first remains constant, then shifts to a longer wavelength. Furthermore, a closer observation reveals that upon D increase the energies associated to the hybrid modes tend to approach one another when D increases.

The FP-like mode at position 2 and the FP mode at position 4 display the typical feature of TE-TM splitting as a function of incident angle, and the evolution with the parameter of D. The onsets of the TE-TM splittings of them shift to small angles with the increase of D, resulting in much larger splittings for large angle incidence. Similarly, the TPP-like mode at position 3 is not affected by the incident angle, no TE-TM splitting happens. Besides, an additional cavity mode is observed when the value of D reaches 600 nm [see Fig. 7(c)].

V. STRAIN SENSING

The coupling between the TPP and FP modes can be explored for the application of strain sensing considering that the FP mode is highly sensitive to the change of the distance between two DBR stacks, D. Optical strain sensors have attracted considerable attention because of their distinct advantages including immunity to electromagnetic interference and no risk of electric shock in biomedical applications [50,51], they have been widely used in precision measurement scenarios. Here, the sensing function of the proposed structure can be realized through an internal strain caused by force, generating a displacement of $GDBR_2$ and consequently a change in D. In turn, small
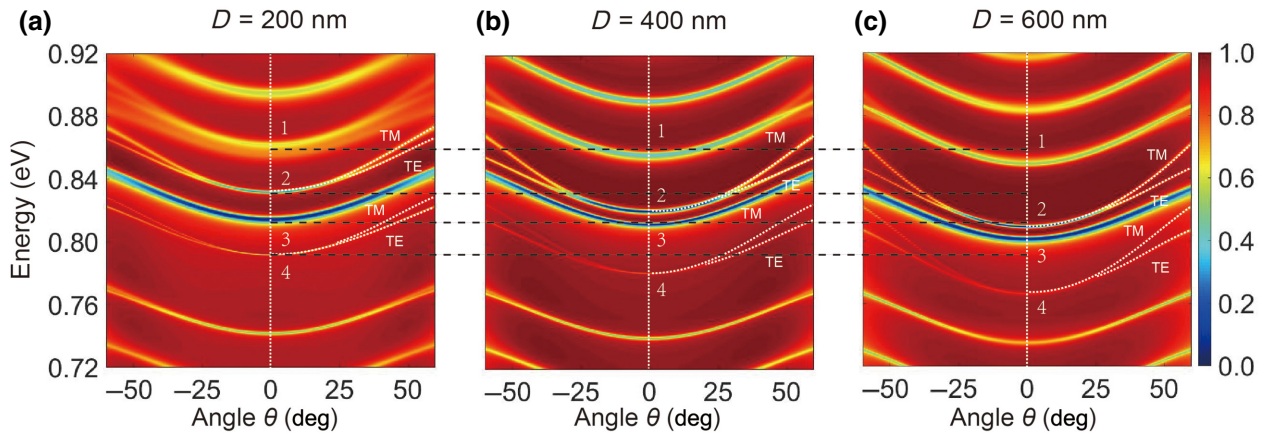

FIG. 7. Angular-resolved reflectance spectra mapping under TE- and TM-polarization pump when $D = 200$ nm (a); 400 nm (b); and 600 nm (c). In (a), positions 1 to 4 correspond to FP cavity mode, FP-like mode, TPP-like mode, and FP cavity mode, respectively. In (b),(c), positions from 1 to 4 correspond to the same modes. The black dashed lines show the shifting of different modes.

variations in D can be detected by monitoring the spectral optical response of the structure.

Figure 8(a) shows the reflectance spectra of the structure for various values of D. We observe that the variation of D almost has no influence on the TPP mode, but the FP mode shifts to longer wavelengths over a large range as D increases. Figure 8(b) plots the change of the FP mode's central wavelength, $\Delta\lambda$, as a function of the corresponding strain parameter, $R = \Delta D/L$ (L is the total length of the device). A near-to-linear relationship between R and λ is observed. Here, we assume that the strain occurs only in the material bounded by the DBR regions. This is a valid approximation for cases where the medium between the DBRs has a small Young's modulus compared to the materials forming the DBRs, as the case studied here. The calculated sensitivity ($S = \Delta\lambda/\Delta R$) reaches 1.77 pm/$\mu\varepsilon$, which ranks the present structure among the most sensitive strain sensors when compared with those reported in the literature [52–56].
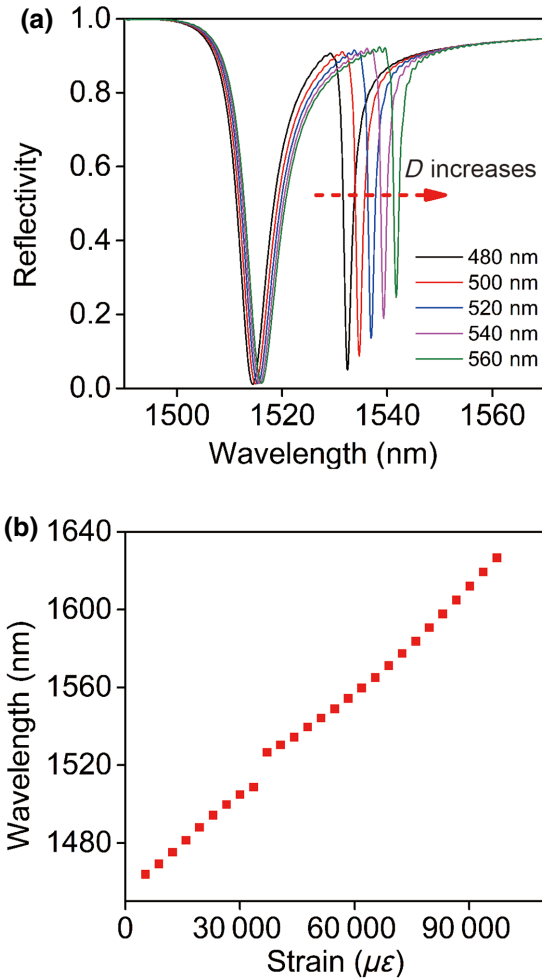

FIG. 8.   Sensing performance of the strain sensor: (a) typical reflectance spectra with different values of D, the red dashed arrow indicates the shifting of the spectrum; (b) the shift of the FP mode as a function of the strain.

VI. CONCLUSIONS

In summary, we propose a 1D photonic crystal heterostructure design, which favors the strong coupling between the TPP and FP modes. Since the coexistence of those types of resonances, such strong interaction supports multichannel light trapping and strong field localization, as well as some other interesting phenomena including mode hybridization, energy exchange channels, and improved light-absorption performance of the system. The strong coupling between the TPP and FP modes enables a remarkable frequency splitting up to 9.298 meV. More significantly, through the characterization of angular-resolved reflectance spectra mapping, we find the coupling between the TPP and FP modes can be dynamically tuned by modifying the physical parameters of D_s and D.

The proposed structure also allows us to completely investigate the TE-TM splitting, the results indicate that only the FP-like mode and FP cavity mode display splittings with the changing of incident angle, no splitting is observed for TPP-like mode, which is caused by the coupling nature between those modes and excitation light. The observation is very significant for the investigation of channeling of polaritons below metallic structure caused by the hybridization of the Tamm states and cavity polaritons [57]. Furthermore, the TE-TM splitting increases with the incident angle, and the increases of D_s and D drive the onset of splitting to shift to small angles.

We also explore the strain-sensing capabilities of this structure by monitoring the spectral shift of the supported optical modes as a function of the distance between the two DBR stacks. We show that the structure exhibits a large sensitivity of 1.77 pm/$\mu\varepsilon$, which ranks among the highest values reported. Thus, the proposed structure could be promising for developing highly accuracy integrated force sensors.

[1] A. F. Koenderink, A. Alú, and A. Polman, Nanophotonics: Shrinking light-based technology, Science **348**, 516 (2015).

[2] W. L. Barnes, A. Dereux, and T. W. Ebbesen, Surface plasmon subwavelength optics, Nature **424**, 824 (2003).

[3] S. Rajabali, E. Cortese, M. Beck, S. D. Liberato, J. Faist, and G. Scalari, Polaritonic nonlocality in light-matter interaction, Nat. Photon. **15**, 690 (2021).

[4] D. S. Dovzhenko, S. V. Ryabchuk, Y. P. Rakovich, and I. R. Nabiev, Light-matter interaction in the strong coupling regime: Configurations, conditions, applications, Nanoscale **10**, 3589 (2018).

[5] J. McKeever, A. Boca, A. D. Boozer, J. R. Buck, and H. J. Kimble, Experimental realization of a one-atom laser in the regime of strong coupling, Nature (London) **425**, 268 (2003).

[6] T. Volz, A. Reinhard, M. Winger, A. Badolato, K. J. Hennessy, E. L. Hu, and A. Imamoglu, Ultrafast all-optical switching by single photons, Nat. Photon. **6**, 605 (2012).

[7] R. Sarma, N. Nookala, K. J. Reilly, S. Liu, D. d. Ceglia, L. Carletti, M. D. Goldflam, S. Campione, K. Sapkota, H. Green, G. T. Wang, J. Klem, M. B. Sinclair, M. A. Belkin, and I. Brener, Strong coupling in all-dielectric intersubband polaritonic metasurfaces, Nano Lett. **21**, 367 (2021).

[8] H. Zhang, J. Sun, J. Yang, I. D. Leon, R. P. Zaccaria, H. Qian, H. Chen, G. Wang, and T. Wang, Biosensing performance of a plasmonic-grating-based nanolaser, Prog. Electromagn. Res. **171**, 159 (2021).

[9] H. Zhang, T. Wang, J. Tian, J. Sun, S. Li, I. De Leon, R. P. Zaccaria, L. Peng, F. Gao, X. Lin, H. Chen, and G. Wang, Quasi-BIC laser enabled by high-contrast grating resonator for gas detection, Nanophotonics **11**, 297 (2022).

[10] H. Deng, H. Haug, and Y. Yamamoto, Exciton-polariton Bose-Einstein condensation, Rev. Mod. Phys. **82**, 1489 (2010).

[11] E. Mavrona, S. Rajabali, F. Appugliese, J. Andberger, M. Beck, G. Scalari, and J. Faist, THz ultrastrong coupling in an engineered Fabry-Perot cavity, ACS Photonics **8**, 2692 (2021).

[12] E. Will, L. Masters, A. Rauschenbeutel, M. Scheucher, and J. Volz, Coupling a Single Trapped Atom to a Whispering-Gallery-Mode Microresonator, Phys. Rev. Lett. **126**, 233602 (2021).

[13] H. Yu, Y. Peng, Y. Yang, and Z. Y. Li, Plasmon-enhanced light-matter interactions and applications, npj Comput. Mater. **5**, 45 (2019).

[14] D. K. Gramotnev and S. I. Bozhevolnyi, Plasmonics beyond the diffraction limit, Nat. Photon. **4**, 83 (2010).

[15] F. Kong, K. Li, B.-I. Wu, H. Huang, H. Chen, and J. Kong, Propagation properties of the SPP modes in nanoscale narrow metallic gap, channel, and hole geometries, Prog. Electromagn. Res. **76**, 449-466 (2007).

[16] J. N. Anker, W. P. Hall, O. Lyandres, N. C. Shah, J. Zhao, and R. P. van Duyne, Biosensing with plasmonic nanosensors, Nat. Mater. **7**, 442 (2008).

[17] A. G. Brolo, E. Arctander, R. Gordon, B. Leathem, and K. L. Kavanagh, Nanohole-enhanced Raman scattering, Nano Lett. **4**, 2015 (2004).

[18] C. L. Haynes, A. D. McFarland, and R. P. van Duyne, Surface-enhanced: Raman spectroscopy, Anal. Chem. **77**, 338A (2005).

[19] T. W. Ebbesen, C. Genet, and S. I. Bozhevolnyi, Surface-plasmon circuitry, Phys. Today **61**, 44 (2008).

[20] I. Y. Chestnov, E. S. Sedov, S. V. Kutrovskaya, A. O. Kucherik, S. M. Arakelian, and A. V. Kavokin, One-dimensional Tamm plasmons: Spatial confinement, propagation, and polarization properties, Phys. Rev. B **96**, 245309 (2017).

[21] O. Buchnev, A. Belosludtsev, V. Reshetnyak, D. R. Evans, and V. A. Fedotov, Observing and controlling a Tamm plasmon at the interface with a metasurface, Nanophotonics **9**, 897 (2020).

[22] M. Kaliteevski, I. Iorsh, S. Brand, R. A. Abram, J. M. Chamberlain, A. V. Kavokin, and I. A. Shelykh, Tamm plasmon-polaritons: Possible electromagnetic states at the interface of a metal and a dielectric Bragg mirror, Phys. Rew. B **76**, 165415 (2007).

[23] A. V. Baryshev, K. Kawasaki, P. B. Lim, and M. Inoue, Interplay of surface resonances in one-dimensional plasmonic magnetophotonic crystal slabs, Phys. Rev. B **85**, 205130 (2012).

[24] J. A. Schuller, E. S. Barnard, W. Cai, Y. C. Jun, J. S. White, and M. L. Brongersma, Plasmonics for extreme light concentration and manipulation, Nat. Mater. **9**, 193 (2010).

[25] X. Wang, X. Jiang, Q. You, J. Guo, X. Dai, and Y. Xiang, Tunable and multichannel terahertz perfect absorber due to Tamm surface plasmons with graphene, Photon. Res. **5**, 536 (2017).

[26] P. S. Pankin, S. Y. Vetrov, and I. V. Timofeev, Tunable hybrid Tamm-microcavity states, J. Opt. Soc. Am. B **34**, 2633 (2017).

[27] C. Symonds, G. Lheureux, J. Hugonin, J. Greffet, J. Laverdant, G. Brucoli, A. Lemaitre, P. Senellart, and J. Bellessa, Confined Tamm plasmon lasers, Nano Lett. **13**, 3179 (2013).

[28] G. Lheureux, S. Azzini, C. Symonds, P. Senellart, A. Lemaitre, C. Sauvan, J. P. Hugonin, J. J. Greffet, and J. Bellessa, Polarization-controlled confined Tamm plasmon lasers, ACS Photonics **2**, 842 (2015).

[29] V. Toanen, C. Symonds, J. M. Benoit, A. Gassenq, A. Lemaıtre, and J. Bellessa, Room-temperature lasing in a low-loss Tamm plasmon cavity, ACS Photonics **7**, 2952 (2020).

[30] Z. A. Zaky, A. M. Ahmed, A. S. Shalaby, and A. H. Aly, Refractive index gas sensor based on the Tamm state in a one-dimensional photonic crystal: Theoretical optimisation, Sci. Rep. **10**, 9736 (2020).

[31] N. Li, T. Tang, J. Li, L. Luo, P. Sun, and J. Yao, Highly sensitive sensors of fluid detection based on magneto-optical optical Tamm state, Sens. Actuators B: Chem. **265**, 644 (2018).

[32] Z. Y. Yang, S. Ishii, T. Yokoyama, T. D. Dao, M. G. Sun, P. S. Pankin, I. V. Timofeev, T. Nagao, and K. P. Chen, Narrow band wavelength selective thermal emitters by confined Tamm plasmon polaritons, ACS Photonics **4**, 2212 (2017).

[33] Z. Wang, J. K. Clark, Y. L. Ho, S. Volz, H. Daiguji, and J. J. Delaunay, Ultranarrow and wavelength-tunable thermal emission in a hybrid metal-optical Tamm state structure, ACS Photonics **7**, 1569 (2020).

[34] P. Das, S. Mukherjee, M. Wan, and S. K. Ray, Optical Tamm state aided room-temperature amplified spontaneous emission from carbon quantum dots embedded one-dimensional photonic crystals, J. Phys. D: Appl. Phys. **52**, 035102 (2018).

[35] R. P. Stanley, R. Houdré, U. Oesterle, and M. Ilegems, Coupled semiconductor microcavities, Appl. Phys. Lett. **65**, 2093 (1994).

[36] N. M. Sundaresan, Y. Liu, D. Sadri, L. J. Szöcs, D. L. Underwood, M. Malekakhlagh, H. E. Türeci, and A. A. Houck, Beyond Strong Coupling in a Multimode Cavity, Phys. Rev. X **5**, 021035 (2015).

[37] A. Graf, L. Tropf, Y. Zakharko, J. Zaumseil, and M. C. Gather, Near-infrared exciton-polaritons in strongly coupled single-walled carbon nanotube microcavities, Nat. Commun. **7**, 13078 (2016).

[38] T. Mikhailova, S. Tomilin, S. Lyashko, M. Kozhaev, A. Shaposhnikov, A. Karavainikov, V. Berzhansky, and V. Belotelov, Tamm plasmon-polaritons and Fabry-Perot excitation in a magnetophotonic structure, Opt. Mat. Express **12**, 685 (2022).

[39] J. Hu, W. Liu, W. Xie, W. Zhang, E. Yao, Yan Zhang, and Q. Zhan, Strong coupling of optical interface modes in a 1D topological photonic crystal heterostructure/Ag hybrid system, Opt. Lett. **44**, 5642 (2019).

[40] Y. M. Qing, H. F. Ma, and T. J. Cui, Investigation of strong multimode interaction in a graphene-based hybrid coupled plasmonic system, Carbon **145**, 596 (2019).

[41] M. L. Garcia, Y. L. D. Ho, M. P. C. Taverne, L. F. Chen, M. M. Murshidy, A. P. Edwards, M. Y. Serry, A. M. Adawi, J. G. Rarity, and R. Oulton, Efficient out-coupling and beaming of Tamm optical states via surface plasmon polariton excitation, Appl. Phys. Lett. **104**, 231116 (2014).

[42] D. Das, P. Boyer, and J. Salvi, Refractive index sensor based on a Tamm Fabry–Perot hybrid resonance, Appl. Opt. **60**, 4738 (2021).

[43] R. Brückner, M. Sudzius, S. I. Hintschich, H. Fröb, V. G. Lyssenko, M. A. Kaliteevski, I. Iorsh, R. A. Abram, A. V. Kavokin, and K. Leo, Parabolic polarization splitting of Tamm states in a metal-organic microcavity, Appl. Phys. Lett. **100**, 062101 (2012).

[44] M. F. Schubert, J. Q. Xi, J. K. Kim, and E. F. Schubert, Distributed Bragg reflector consisting of high- and low-refractive-index thin film layers made of the same material, Appl. Phys. Lett. **90**, 141115 (2007).

[45] M. Kaliteevski, S. Brand, R. A. Abram, I. Iorsh, A. V. Kavokin, and I. A. Shelykh, Hybrid states of Tamm plasmons and exciton polaritons, Appl. Phys. Lett. **95**, 251108 (2009).

[46] Y. Zheng, Y. Wang, J. Luo, and P. Xu, Optical Tamm states in photonic structures made of inhomogeneous material, Opt. Commun. **406**, 103 (2018).

[47] G. Khitrova, H. Gibbs, M. Kira, S. W. Koch, and A. Scherer, Vacuum Rabi splitting in semiconductors, Nat. Phys. **2**, 81 (2006).

[48] W. L. Zhang and Y. J. Rao, Optical Tamm state polaritons in a quantum well microcavity with gold layers, Chin. Phys. B **21**, 057107 (2012).

[49] F. Manni, K. G. Lagoudakis, T. K. Paraïso, R. Cerna, Y. Léger, T. C. H. Liew, I. A. Shelykh, A. V. Kavokin, F. Morier-Genoud, and B. Deveaud-Plédran, Spin-to-orbital angular momentum conversion in semiconductor microcavities, Phys. Rev. B **83**, 241307(R) (2011).

[50] T. Okatani, S. Sekiguchi, K. Hane, and Y. Kanamori, Surface-plasmon-coupled optical force sensors based on metal-insulator-metal metamaterials with movable air gap, Sci. Rep. **10**, 14807 (2020).

[51] P. Roriz, O. Frazão, A. B. Lobo-Ribeiro, J. L. Santos, and J. A Simões, Review of fiber-optic pressure sensors for biomedical and biomechanical applications, J. Biomed. Opt. **18**, 050903 (2013).

[52] L. Donga, T. Gangb, C. Biana, R. Tonga, J. Wanga, and M. Hu, A high sensitivity optical fiber strain sensor based on hollow core tapering, Opt. Fiber Technol. **56**, 102179 (2020).

[53] I. M. Pryce, K. Aydin, Y. A. Kelaita, R. M. Briggs, and H. A. Atwater, Highly strained compliant optical metamaterials with large frequency tunability, Nano Lett. **10**, 4222 (2010).

[54] E. P. Chan, J. J. Walish, A. M. Urbas, and E. L. Thomas, Mechanochromic photonic gels, Adv. Mater. **25**, 3934e3947 (2013).

[55] L. Minati, A. Chiappini, C. Armellini, A. Carpentiero, D. Maniglio, A. Vaccari, L. Zur A. Lukowiak, M. Ferrari, and G. Speranza, Gold nanoparticles 1D array as mechanochromic strain sensor, Mater. Chem. Phys. **192**, 94e99 (2017).

[56] K. Yang, F. Yin, D. Xia, H. Peng, J. Yanga, and W. Yuan, A highly flexible and multifunctional strain sensor based on a network-structured MXene/polyurethane mat with ultra-high sensitivity and a broad sensing range, Nanoscale **11**, 9949 (2019).

[57] T. C. H. Liew, A. V. Kavokin, T. Ostatnický, M. Kaliteevski, I. A. Shelykh, and R. A. Abram, Exciton-polariton integrated circuits, Phys. Rev. B **82**, 033302 (2010).